J Adv Ceram

Research Article

Excellent high-temperature strength of (HfZrTiTaNb)C high-entropy carbide diffusion-bonded joint via *in-situ* alloying of Ni/Nb/Ni composite interlayer

Ruijie Mu[1], Ying Wang[1,2,✉], Shiyu Niu[1], Kongbo Sun[1], Zhenwen Yang[1,2,✉]

Cite this article: Mu R, Wang Y, Niu S, et al. *J Adv Ceram* 2025, **14**(1): 9221010. https://doi.org/10.26599/JAC.2024.9221010

ABSTRACT: To obtain high-entropy carbide (HEC) joints with excellent high-temperature performance, a (HfZrTiTaNb)C HEC joint featuring a direct diffusion-bonded interface with a Nb-based interlayer was successfully fabricated at relatively low temperatures of 1150–1250 °C for 60 min under 10 MPa. Starting from a modified Ni/Nb/Ni composite interlayer with a Nb content of > 64 at%, an alloyed Nb_2Ni layer was constructed *in situ* by accelerating the directional diffusion of Ni atoms from the high-entropy interface into the remaining pure Nb through the Ni–Nb eutectic liquid. Moreover, the excess liquid phase was squeezed out of the bonding region, ensuring the absence of Ni-based compounds. Leveraging the intrinsic interfacial stability and sluggish diffusion effect, the HEC with its original lattice structure, was capable of developing diffusion bonding with the Nb_2Ni layer instead of interacting with the liquid phase. The high reliability of the HEC/Nb_2Ni bonded interface was confirmed by the coherence of $(1\bar{1}3)_{HEC}//(141)_{Nb_2Ni}$ and a calculated lattice misfit of 0.044. The HEC joint had a high room-temperature strength of 174 MPa because of the homogenous Nb_2Ni layer, which exhibited nanohardness (15.2±1.5 GPa) and an elastic modulus of 219.9±17.5 GPa. Furthermore, the strength of the HEC joint did not decrease at 1000 °C, increasing by ~49% over that of HEC/Ni/HEC diffusion-bonded joints, which have stringent surface flatness requirements. This suggested that the HEC/Nb_2Ni interface had excellent resistance to high-temperature softening, even though it was invariably the initial failure location. This work is informative for designing bonding structures and preparing HEC components.

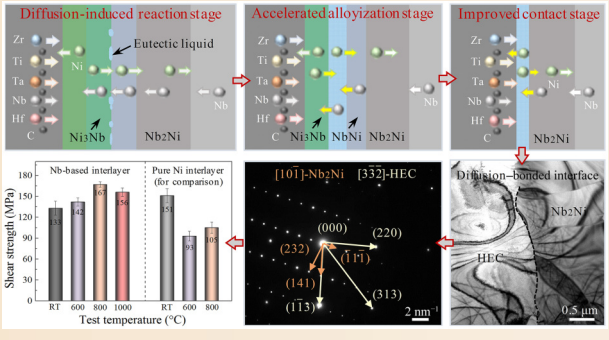

KEYWORDS: high-entropy ceramic; diffusion bonding; *in situ* alloyed interlayer; mechanical properties

1 Introduction

High-entropy carbides (HECs) are generally solid solution phases with a mixing entropy higher than 1.5*R* (*R* is the gas constant) obtained by introducing at least four or five transition metal elements [1,2]. High conformational entropy induces unique characteristics in HECs, i.e., a structural lattice distortion effect, sluggish kinetic diffusion, and a cocktail effect on performance [3,4]. HECs with exceptional mechanical properties and ultrahigh thermal stability are promising for extreme environments in aerospace crafts, hypersonic vehicles, nuclear reactors, and high-speed cutting tools [5–8]. As structural ceramics, sintered HEC bulk materials have difficulty directly obtaining large sizes and complex shapes, such as hollow or stepped components, owing to their limited furnace capacity and essential axial pressurization [9,10]. Fabricating reliable HEC joints that match the excellent performance of HEC substrates [5,9] is crucial for promoting their engineering application. In this process, the endurance temperature of HEC joints requires continuous improvement to allow for applications in more extreme thermal environment components [7]. Along with studies on the bonding interface between the HEC and itself, integrated structures and the interfacial response of the HEC with metallic materials have also attracted attention.

Considering the inherent brittleness of HECs, their joints for high-temperature service could be attained by sinter bonding [11,12], diffusion bonding [13–15], brazing [16–19], transient liquid phase [20], etc. Among them, diffusion bonding is suitable for fabricating high-performance joints [21], where the direct metallurgical bonding of the interfaces relies on effective elemental diffusion at high temperatures. According to reports on conventional carbides, favorable interfacial interdiffusion could be accomplished with elevated bonding temperatures and improved contact through the introduction of soft metals. For example,

[1] Tianjin Key Laboratory of Advanced Joining Technology, School of Materials Science and Engineering, Tianjin University, Tianjin 300350, China. [2] Key Laboratory of Advanced Ceramics and Machining Technology, Ministry of Education, Tianjin 300350, China.

✉ Corresponding authors. E-mail: Y. Wang, tjuywang@163.com; Z. Yang, tjuyangzhenwen@163.com

Received: August 29, 2024; Revised: November 12, 2024; Accepted: November 27, 2024

ZrC_x joints with diffusion bonding with Ti/Zr/Ti and Ti/Ta/Ti multilayers at 1400 °C under 20 MPa presented strengths of 157 and 122.5 MPa, respectively [13,14]. ZrC–SiC joints could be achieved by accelerated atomic diffusion through a heat source provided by a pulsed current when a 30 μm thick Ti foil was used at 1300 °C [22]. Departing from conventional carbides, the larger potential energy fluctuation in the distortion lattices of HECs increases the difficulty of atomic migration [3,23]. Previous studies demonstrated that direct diffusion bonding of HEC required bonding temperatures of up to 1500 °C and a pressure of 30 MPa [15]. Therefore, for high-entropy interfaces under the sluggish diffusion effect, excessive-high process conditions would be required to accelerate interfacial diffusion if homogeneous carbide-based bonding structures of HECs that withstand high-temperature service environments are considered to be realized by existing solid-phase diffusion bonding approaches.

To reduce the bonding process conditions of HECs, especially the bonding temperature, the introduction of liquid phases at the interfaces was necessary to accelerate interfacial diffusion. The brazed joints were developed from solidified liquid alloys that fill the interstices between two HEC substrates under less pressure. From the microstructures of HEC joints brazed with TiNi–20Nb (at%) [16], TiNi [17], TiZrNiCu [18], and BNi_2 [19] fillers, these filler alloys frequently develop low melting point intermetallic compounds present at the bonding interfaces or suffer from eutectic transitions (at ~1118 °C for the TiNi-based alloy fillers), leading to weakened high-temperature durability and a high risk for joint failure. The shear strengths of HEC joints with a TiNi–20Nb (at%) filler were 167 and 137 MPa when tested at room temperature (RT) and 800 °C, respectively [16]. Even when a transient liquid phase generated from Ni and Nb with a thickness ratio of only 2/125 was applied, the liquid phase containing abundant Ni atoms at the interface between traditional binary carbides (ZrC, HfC, and TaC) and the Ni/Nb/Ni multilayer could not completely disappear isothermally at 1400 °C [20]. The residual liquid phase in the ceramic joints inevitably becomes a constraint to further increase the serviceable temperature of the joints. Improving the service temperature of HEC joints bonded at relatively low temperatures through the design of assisted liquid phases and process adjustments is still challenging.

On the basis of the inherent high-entropy effects in HECs oriented to high-temperature applications, *in situ* alloying of refractory metals and interfacial diffusion accelerated by a eutectic liquid phase were proposed to prepare HEC joints with refractory metal-based interlayers at decreased bonding temperatures. In this process, a designed Ni–Nb eutectic liquid phase accelerated the directed Ni atomic diffusion induced by the disparity in entropy on both sides of the interface between the HEC and the Ni/Nb/Ni composite interlayer in this work, whereas a large bonding pressure was applied to permit timely extrusion of the excess liquid phase and maintain tight interfacial contact and the resulting interdiffusion of multiple elements. The amount of the liquid phase and its isothermal duration could be optimized by adjusting the Ni/Nb proportions. According to reports that refractory metals can serve as high-temperature skeletons [24] and reaction barrier layers [25], retaining a refractory Nb-based interlayer with a high melting point in HEC joints is expected to result in low-temperature bonding of HECs for high-temperature service.

Herein, a Ni/Nb/Ni composite interlayer was modified to fabricate a (HfZrTiTaNb)C HEC joint featuring a direct bonding interface with a diffusion-induced *in situ* alloyed Nb-based interlayer at 1150–1250 °C under 10 MPa. The interfacial microstructures of joints under the influence of different bonding temperatures and Ni/Nb ratios were analyzed. The formation mechanism of the bonding interface between the HEC and the Nb-based interlayer was revealed. Additionally, the shear strength and corresponding high-temperature failure behavior of HEC diffusion-bonded joints were evaluated. The results are instructive for designing bonding structures of HEC joints and the preparation of HEC components.

2 Materials and methods

A high-entropy carbide ceramic with representative components of (HfZrTiTaNb)C, which was fabricated via ball milling and hot-press sintering, was selected as the substrate. The detailed process and parameters can be found in our previous work [15]. Sintered HECs have good physical and mechanical properties, including high relative density (> 99%), high Vickers hardness (24 GPa), and high flexural strength (494 MPa). Before diffusion bonding, the HEC was cut into substrates with dimensions of 10 mm × 10 mm × 5 mm and 5 mm × 5 mm × 5 mm by electrical discharge machining. Symmetric Ni/Nb/Ni composite interlayers with areas of 6 mm × 6 mm were created by stacking commercial foils of pure Nb with thicknesses of 60 μm and pure Ni foils with thicknesses of Ni of 10, 20, and 30 μm. The Ni/Nb/Ni composite interlayers with different thicknesses of Ni were named Nb-1, Nb-2, and Nb-3. The surfaces of the HEC and each foil were ground and ultrasonically cleaned in acetone for 15 min. Then, the Ni/Nb/Ni composite interlayer was assembled between the HEC substrates. The assemblies in a sandwich structure were placed horizontally on the indenter of a furnace and preloaded with a load of 0.2 MPa. Schematic diagrams of the HEC joint and diffusion–bonding assembly are shown in Fig. 1. When the vacuum degree was less than 10^{-4} Pa, the heating process was triggered, and the curves of the bonding temperature and pressure are shown in Fig. 1. The furnace was heated at a rate of 20 °C/min to 400 °C. The temperature was increased at 10 °C/min to bonding temperatures of 1150–1250 °C while the pressure was maintained at 10 MPa. After bonding for 60 min, the assemblies were cooled to 400 °C at 5 °C/min, and the pressure was slowly reduced until the indenter was withdrawn. The joints were kept in the furnace until the furnace temperature was no higher than 70 °C.

The microstructures of the joints were observed by a scanning electron microscope (SEM; JSM-7800F, JEOL, Japan) under an accelerating voltage of 15 kV. An energy dispersive spectrometer (EDS; Octane Plus of EDAX, AMETEK, USA) was used for chemical composition analysis. The bonding interface zone of the joint was precisely extracted by a focused ion beam instrument (FIB; Helios NanoLab 600i, FEI, USA), and a transmission electron microscope (TEM; JEM-2100F, JEOL, Japan) was further used to obtain the interfacial elemental distribution at the

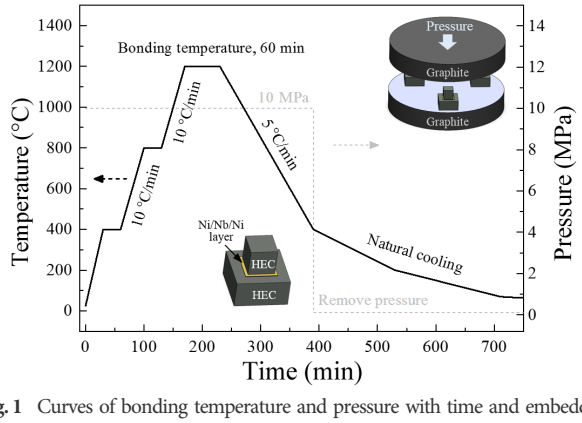

Fig. 1 Curves of bonding temperature and pressure with time and embedded HEC joint and its assembly schematic diagrams.

nanoscale and selected area electron diffraction (SAED) patterns of the phases.

The shear strengths of HEC joints were evaluated at RT and elevated temperatures of 600, 800, and 1000 °C in air via a uniaxial machine (E45.106, MTS, China) with a loading rate of 0.2 mm/min. The shear tests were performed using single-lap offset flat-back samples, and a schematic diagram is given in Fig. S1 in the Electronic Supplementary Material (ESM), similar to that in Refs. [16, 18]. Before loading, the sample was heated to the test temperature for no more than 30 min at a heating rate of 10 °C/min, after which it was soaked for 10 min until reaching thermal equilibrium. The shear fracture was analyzed via an X-ray diffractometer (XRD; D8 Advanced, Bruker, Germany) to identify phases in the joint microstructure. The XRD scan was performed with Cu Kα radiation under a voltage of 40 kV and a current of 40 mA. A nanoindenter tester (Agilent G200, KLA, USA) was used to quantify the nanohardness and elastic modulus of different phases in the HEC joints, during which the loads had a controlled indentation depth of ~0.26 nm and a holding time of 10 s. The estimated Poisson's ratios of the HEC and the alloyed Nb interlayer were 0.2 [26] and 0.3 [27], respectively. The values of the mechanical properties were averaged over at least three measurements, and the error bars were taken from the standard deviation.

3 Results and discussion

3.1 Typical microstructures of HEC joints bonded with Ni/Nb/Ni composite interlayer

The SEM image in Fig. 2(a) shows that the original (HfZrTiTaNb)C high-entropy ceramic was a single solid-solution phase. The TEM analysis in Figs. 2(b) and 2(c), including the HAADF-STEM image, the corresponding SAED pattern, and the high-resolution TEM (HRTEM) image, proved that the HEC lattice was a face-centered cubic (FCC) structure with an (022) interplanar distance of 1.57 Å. EDS results revealed that the HEC contained 47.99% C, 12.01% Hf, 8.38% Zr, 9.82% Ti, 11.84% Ta, and 9.96% Nb (at%). As shown in Figs. 2(d)–2(i), the distribution maps of each element in the HEC displayed consistent homogeneity.

Figure 3(a) shows the typical microstructure of the HEC joint bonded with the Nb-1 interlayer at 1250 °C for 60 min under 10 MPa, and the enlarged interfacial region can be seen in Fig. 3(b). No cracks or pores were observed in the diffusion-bonded joint. An Nb-based zone (NZ) was in the middle of the joint, and the formed interface between the NZ and the HEC matrix was well bonded. According to the detailed chemical compositions in Table 1, small amounts of Ni and Nb atoms diffused into the HEC near the interface, and the HEC maintained an intrinsic multicomponent solid solution (position A). The NZ layer in the joint mainly consisted of the Nb_2Ni phase (position B) and a small quantity of transition metal atoms from the HEC. A blocky $(Nb,Ta)_2Ni$ phase (position C) with a slightly higher Ta content (5.27 at%) than the Nb_2Ni phase (2.16 at%) was found. The Nb(s,s) block phases (labeled D in Fig. 3(b)) were randomly precipitated in the Nb_2Ni layer, which was in agreement with the refined phase diagram of the Ni-Nb binary system [28,29]. The result of EDS line scanning in Fig. 3(c) shows a narrow concentration variation distance of ~1.5 μm from the HEC to the Nb_2Ni, which suggested that the metallurgical bonding between

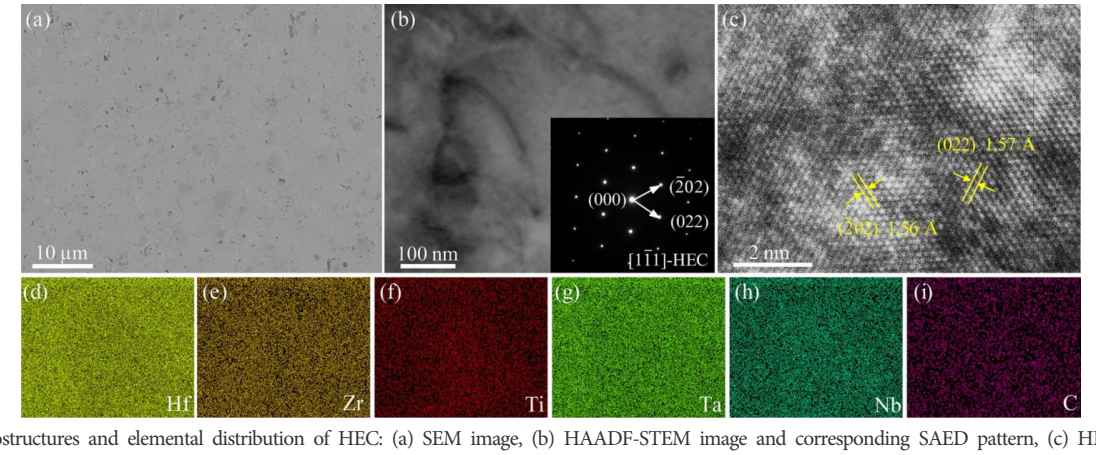

Fig. 2 Microstructures and elemental distribution of HEC: (a) SEM image, (b) HAADF-STEM image and corresponding SAED pattern, (c) HRTEM image, and (d–i) EDS mappings of (b).

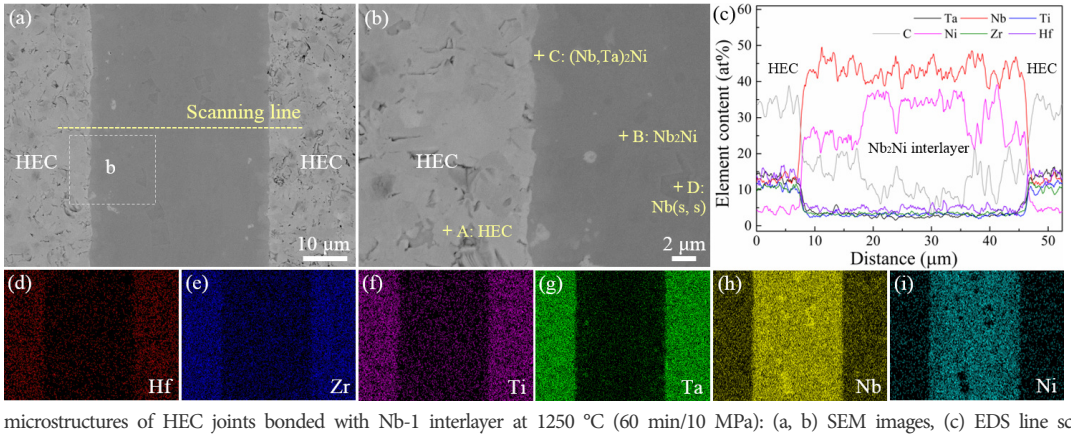

Fig. 3 Typical microstructures of HEC joints bonded with Nb-1 interlayer at 1250 °C (60 min/10 MPa): (a, b) SEM images, (c) EDS line scanning results, and (d–i) element distribution mappings.

the Nb_2Ni and HEC originated from their direct interdiffusion, whereas the sluggish diffusion originating from the HEC resulted in a limited atomic diffusion distance. As shown in Figs. 3(d)–3(i), despite the aggregated Nb in the Nb(s,s) phases, the elemental distribution in the other phases in the joint was uniform.

Therefore, benefiting from the high-entropy effects of HEC, the introduced Ni was driven into the Nb rather than interacting with the ceramic substrate under the gradient of configurational entropy from the HEC to Nb, successfully achieving the HEC diffusion-bonded joint with an *in situ* formed Nb-rich interlayer. Notably, the preparation of the HEC joints in this work started from the optimized Ni/Nb/Ni composite interlayer, yielding an interfacial microstructure free of eutectic compounds. This distinguished it from the reported joints with Ni–Nb alloy brazing fillers or added Ni/Nb composite layers, where the inevitable compounds existed after the melting-solidification process of the Ni–Nb alloys [30,31], leading to the results of the current studies consistently lacking information about the Nb_2Ni phase [20,32]. Similarly, this is the reason why the prefabrication of homogeneous alloyed Nb foils was not practical with conventional casting approaches.

Figure 4 presents the TEM analysis of the bonding interface of the HEC and NZ in the joint. The bright field TEM images in Figs. 4(a) and 4(b) reveal direct metallurgical bonding at the HEC/NZ interface without carbides or complex compounds. The SAED patterns of the interfacial zone in Fig. 4(c) revealed that the HEC was a single FCC solid solution structure with a lattice parameter of a = 4.59 Å, similar to the results in Figs. 2(b) and 2(c). In NZ, the $(\bar{1}1\bar{1})$ interplanar distance of the Nb_2Ni phase was measured as 6.794 Å, and its crystal structure was consistent with the $Fd\bar{3}m$ (227) cubic structure (PDF#21-0587). The calculated lattice parameter a was 11.77 Å, which was similar to the results of Zhao *et al.* [31]. Additionally, the coherence of $(141)_{Nb_2Ni}//(1\bar{1}3)_{HEC}$ was distinct at the interface between the HEC and the formed Nb_2Ni phase along the $[10\bar{1}]_{Nb_2Ni}//[3\bar{3}\bar{2}]_{HEC}$ zone axis. The lattice misfit δ was calculated as 0.044 on the basis of the equation reported by Zheng *et al.* [33], which confirmed the reliable HEC/NZ bonding structure in the joint. Figure 4(d) shows the line distribution of each element from the HEC to the Nb_2Ni phase. A significant concentration gradient of metal elements was observed on both sides of the interface. The diffusion distance of the Nb atoms into the HEC was greater than that of the Ni atoms. The intense peaks of Ti, Hf, and Zr appeared in the HEC adjacent to the bonding interface, whereas the Ta diffused across the interface and presented an increased intensity in Nb_2Ni phase. The diffusive migration of Ta in the HEC into the Nb_2Ni layer was probably attributed to the similar valence electronic structure and the unlimited solid solubility between the Ta and Nb atoms, despite the diffusion rate of Ta in the HEC being lower than that of Ti, Hf, and Zr. Therefore, the formation of the bonding interface in the HEC joint depended on the interdiffusion between the Ta atom in the HEC and the Nb_2Ni layer *in situ* obtained by the Ni/Nb/Ni composite interlayer.

Table 1 Detailed chemical composition of each phase labeled A to D in Fig. 3 (Unit: at%)

Position	Hf	Zr	Ti	Ta	Nb	Ni	C	Possible phase
A	13.26	10.34	10.34	13.05	12.26	1.31	39.44	HEC
B	2.74	1.73	1.28	2.16	59.68	32.41	—	Nb_2Ni
C	2.28	2.70	2.78	5.27	54.42	32.55	—	$(Nb,Ta)_2Ni$
D	3.67	3.14	1.41	1.17	84.93	5.68	—	Nb(s,s)

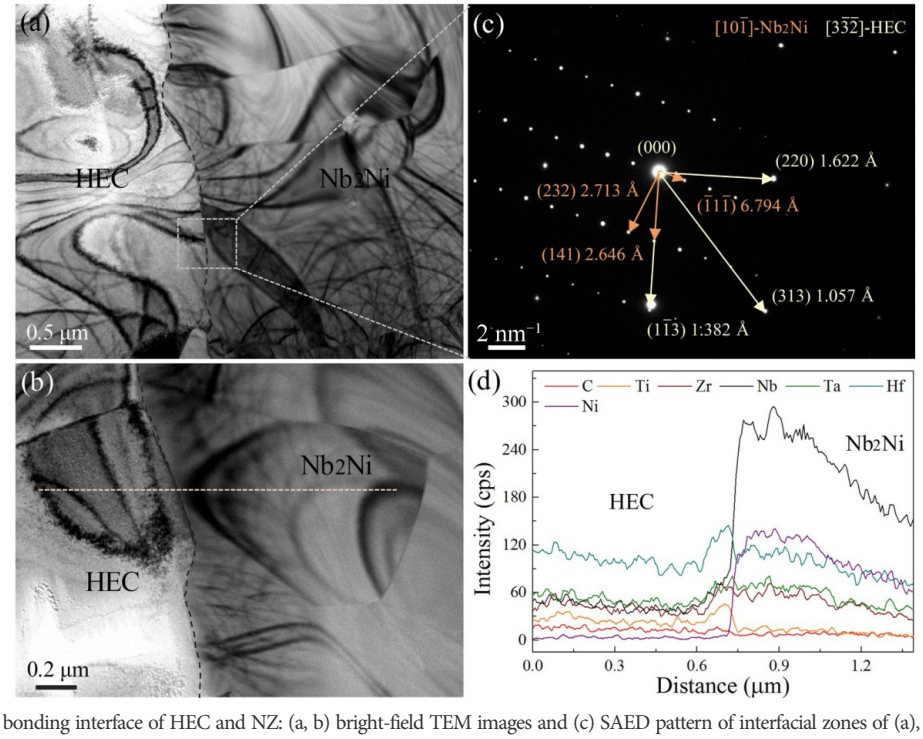

Fig. 4 TEM analysis of bonding interface of HEC and NZ: (a, b) bright-field TEM images and (c) SAED pattern of interfacial zones of (a), (d) element distributions along line marked in (b).

3.2 Effect of the diffusion bonding process on the microstructures of HEC joints bonded with a Ni/Nb/Ni composite interlayer

Figures 5(a)–5(c) show the microstructures of the HEC joints bonded with the Nb-1 interlayer at different temperatures (60 min/10 MPa), and the corresponding interfacial zones marked by gray frame lines are enlarged in Figs. 5(d)–5(f). The interfacial microstructures in the joints were all defect-free. With increasing bonding temperature, the bonding interface evolved from HEC/Ni_3(Nb,Ta) to HEC/Nb_2Ni because the Ni-based phases disappeared at 1200 °C, and full alloying of the initial pure Nb layer into the Nb_2Ni layer occurred at 1250 °C. Table 2 lists the chemical compositions of the phases labeled A to F in Fig. 5. At the lower bonding temperature of 1150 °C, as shown in Figs. 5(a) and 5(d), the effective bonding in the joint depended on the HEC/Ni-based zone (IZ) interface because a symmetrical microstructure, including the NZ and the IZ formed on both sides of the pure Nb layer. The IZ layer consisted of the Ni_3Nb layer and the Ni–Nb eutectic compounds, which preferentially precipitated upon solidification of the trace Ni–Nb eutectic liquid phase at the Ni/Nb interface. As shown in Table 2, the Ni_3Nb phase contained 1.87 at% Ta and 2.67 at% Hf, and the slightly higher Ta content (4.27 at%) and Hf content (3.92 at%) distinguished the Ni_3(Nb,Ta) phase. The increased transition metal elements in Ni_3(Nb,Ta), especially Ta and Hf, confirmed the slight dissolution of the HEC into the trace liquid phase. On the basis of the Ni–Nb binary equilibrium phase diagram [28,29,34], the bonding temperature of 1150 °C was close to the $Ni_{59.5}Nb_{40.5}$ eutectic temperature (1175 °C). Although Birks and Seebold reported that Nb–Ni samples frequently melted at 1100 °C [35] and that the trace liquid phase was indeed generated at the Ni/Nb interface for a long bonding time of 60 min, the insufficient Ni–Nb eutectic liquid phase in the joint could not deplete the many Ni atoms added.

When the bonding temperature was increased to 1200 °C, the NZ contacted and interdiffused with the HEC, forming the HEC/NZ interface in Figs. 5(b) and 5(e). Compared with the interfacial microstructure in Fig. 5(d), the IZ disappeared because a majority of the Ni atoms were expelled from the interface, as more eutectic liquid phase formed by the intensified eutectic reaction between Ni_3Nb and NiNb extruded under a high bonding pressure of 10 MPa. From the EDS results in Table 2, the Nb_2Ni phase (Position D in Fig. 5) constituted the NZ, and $(Nb,Ta)_2Ni$ (Position F in Fig. 5) was detected in the NZ adjacent to the HEC, which is consistent with the results in Figs. 4(a) and 4(c). Zhao *et al.* [36] reported that the Nb_2Ni phase in the joint probably originated from the peritectoid reaction of Nb_7Ni_6 with the Nb layer. Owing to the limited diffusion distance of residual Ni atoms, part of the initial Nb layer (Position E in Fig. 5) was retained in the center of the joint. As shown in Figs. 5(c) and 5(f), the HEC joint with an entire Nb_2Ni interlayer formed when bonded at the elevated bonding temperature of 1250 °C. This was the consequence of the complete alloying of the Nb layer, which benefited from the broadening of the liquid-phase compositional interval and the accelerated interdiffusion between the Ni and Nb atoms in the joint.

The effects of different Ni thicknesses in the Ni/Nb/Ni composite interlayer on the microstructures of the joints are shown in Figs. 6(a)–6(c) when diffusion bonding was performed at 1200 °C for 60 min under 10 MPa. The increased Ni content implied that the corresponding Ni/Nb ratio increased in the

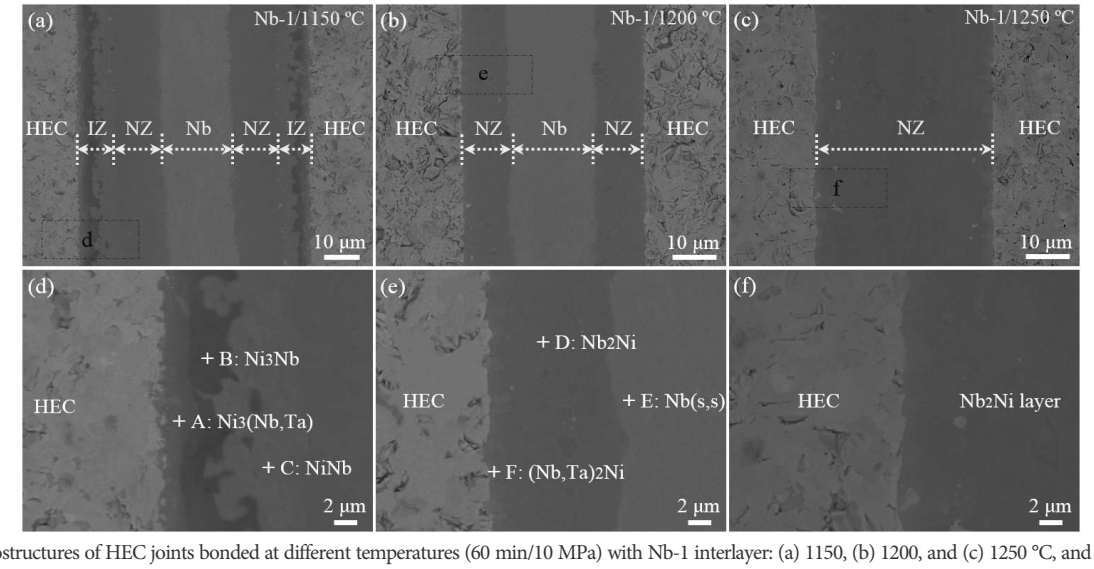

Fig. 5 Microstructures of HEC joints bonded at different temperatures (60 min/10 MPa) with Nb-1 interlayer: (a) 1150, (b) 1200, and (c) 1250 °C, and (d–f) enlarged interfacial zones in (a–c).

Table 2 Detailed chemical composition of each phase labeled A to F in Fig. 5 (Unit: at%)

Positions	Hf	Zr	Ti	Ta	Nb	Ni	Possible phase
A	3.92	2.57	2.18	4.27	19.68	67.38	Ni_3(Nb,Ta)
B	2.67	1.71	1.73	1.87	20.77	71.25	Ni_3Nb
C	2.56	1.52	1.32	1.17	45.48	47.95	NiNb
D	2.74	1.73	1.28	2.16	59.68	32.41	Nb_2Ni
E	2.93	2.30	1.47	1.88	89.10	2.32	Nb(s,s)
F	3.87	2.63	2.94	6.22	53.97	30.37	$(Nb,Ta)_2Ni$

Ni/Nb/Ni composite interlayers, which led to the consumption of the pure Nb layer and a more abundant liquid phase. The NZ/HEC interface in the well-bonded HEC/Nb-1/HEC joint was substituted by the IZ/HEC interface, and the IZ layer even expanded to fill the entire interface in the HEC/Nb-3/HEC joint. Moreover, the percentages of the retained interlayer thickness in the joint to the original thickness of the Ni/Nb/Ni composite interlayers decreased from 51% to 31%. The corresponding interlayer thicknesses of 41, 31, and 37 μm were attributed to the collective result of consumption during the generation and extrusion of the Ni-Nb liquid phase, as well as the compressive deformation of soft foils at the high bonding temperature of 1200 °C under a bonding pressure of 10 MPa.

The enlarged interfacial zones are displayed in Figs. 6(d)–6(f), and the average chemical composition of each phase marked by A to E is listed in Table 3. The diffusion of Nb atoms into the initial pure Ni layer drove the conversion of Ni to Ni_3Nb, corresponding to positions A and B in Fig. 6, and Ni_3Nb served as the matrix phase of the IZ layer, in contrast to the formation of the NZ, which consisted entirely of the Nb_2Ni phase in Figs. 3 and 6(d). At the bonding temperatures, the *in situ* alloyed Nb_2Ni layer (position C in Fig. 6) was continuously supplied with Nb atoms to sustain the generation and extrusion of the eutectic liquid phase, and almost complete consumption was even observed in Figs. 6(c) and 6(f). Owing to the interdiffusion between Ni and Nb, the concentration of Nb atoms in the IZ theoretically decreased from the middle of the IZ interlayer toward the HEC. In the high Nb concentration zone of the IZ, the fine NbNi phase (Position D in Fig. 6) precipitated from the Ni_3Nb phase (Position E in Fig. 6). As shown in Fig. 7, the XRD result on the fracture surface in Fig. 6(c) confirmed the presence of Ni_3Nb, NiNb, and a small amount of the Nb_2Ni phase in the joint, in agreement with the EDS analysis.

At the IZ/HEC interfaces, significant dissolution of the HEC was observed, as shown in Figs. 6(e) and 6(f), whereas a small quantity of the Ni-Nb liquid phase permeated into the HEC along the grain boundaries. This behavior facilitated the release of transition metal elements in the HEC into Ni_3Nb, forming the $Ni_3(Nb,Ta)$ phase. The $Ni_3(Nb,Ta)$ contained significantly increased Hf and Zr contents (Table 3), which was explained by the fact that Hf and Zr have a much higher affinity for Ni than Nb. This result reflected that the liquid phase developed with the addition of Ni improved the interfacial diffusion compared with the direct bonding of the HEC and pure Nb layers. Nevertheless, when excessive Ni was introduced, IZ with complex Ni-based compounds unavoidably formed in the joints, where the HEC/$Ni_3(Nb,Ta)$ interface replaced the HEC/Nb_2Ni interface.

Figure 8 shows a schematic diagram of *in situ* alloyed Nb and the formation mechanism of the diffusion bonding interface with the HEC. The formation process of the diffusion-bonded joint with the Nb-based interlayer can be summarized in three stages: the diffusion-induced reaction stage in Figs. 8(a) and 8(b), the liquid accelerated alloyization stage in Figs. 8(c) and 8(d), and the improved contact stage in Figs. 8(e) and 8(f). The interfacial interdiffusion between Ni and the HEC was difficult, and the diffusion of Ni into Nb occurred easily, resulting in the formation of NiNb and Ni_3Nb reaction layers on both sides of the Ni/Nb interface. Among them, the Ni_3Nb layer was considered to be preferentially generated on the basis of the growth behavior of Ni_3Nb at 820 °C [37]. When the bonding temperature subsequently approached the eutectic temperature of 1175 °C, the NiNb and Ni_3Nb compounds underwent a eutectic reaction at their interface and produced a localized liquid phase. At elevated temperatures, the compounds completely developed a eutectic liquid phase, and then the majority of the liquid phase was

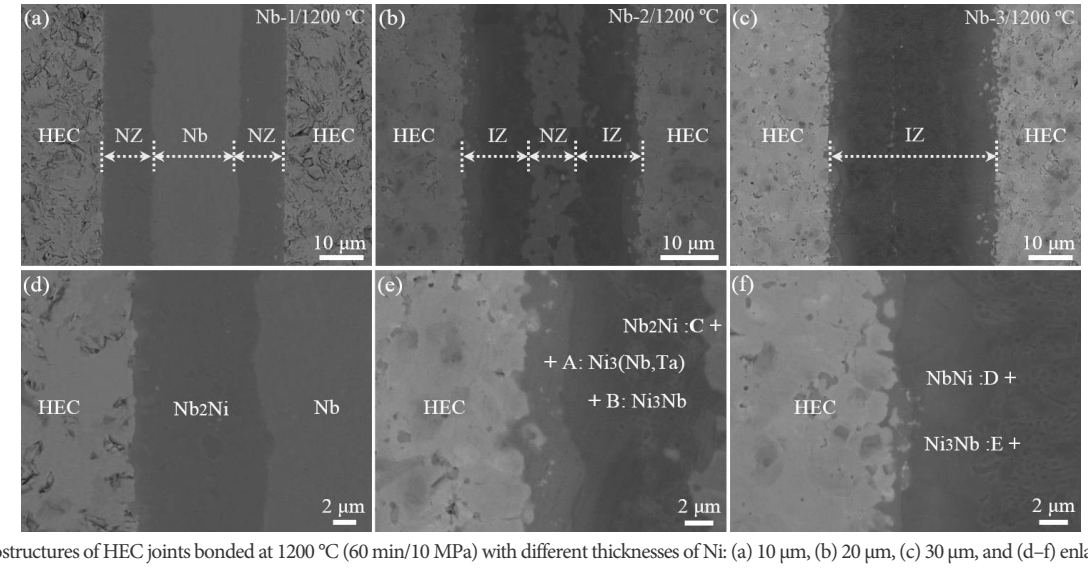

Fig. 6 Microstructures of HEC joints bonded at 1200 °C (60 min/10 MPa) with different thicknesses of Ni: (a) 10 μm, (b) 20 μm, (c) 30 μm, and (d–f) enlarged interfacial zones in (a–c).

Table 3 Average chemical composition analysis of each phase marked by A to E in Fig. 6 (Unit: at%)

Position	Hf	Zr	Ti	Ta	Nb	Ni	Possible phase
A	6.74	4.63	3.17	4.45	12.47	68.54	$Ni_3(Nb,Ta)$
B	3.82	2.12	2.65	1.27	20.08	70.06	Ni_3Nb
C	1.76	2.30	0.53	0.59	61.46	33.36	Nb_2Ni
D	2.36	2.57	1.57	1.02	49.86	42.62	NbNi
E	2.42	1.48	1.46	0.92	23.63	70.09	Ni_3Nb

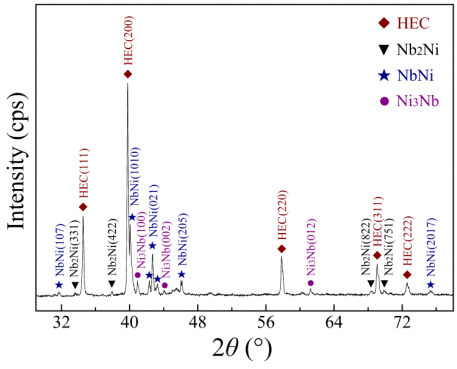

Fig. 7 XRD analysis of fracture surface of HEC/Nb-3/HEC joint at 1200 °C (60 min/10 MPa).

extruded from the interface under diffusion bonding pressure, leaving only a liquid film present, as shown in Figs. 8(c) and 8(d). The liquid film accelerated the atomic exchange between Ni and Nb to yield NiNb and Ni_3Nb compounds, whereas the cyclic process of the eutectic reaction and extrusion of the liquid phase contributed to the persistence of the liquid film.

Simultaneously, the high-entropy effects of HEC contributed to the almost negligible interaction at the interface between the HEC and Ni_3Nb layers, and the HEC near the interface stabilized. For suitable Ni/Nb ratios in the Ni/Nb/Ni composite interlayer, this process resulted in rapid *in situ* alloying of the high-melting-point Nb layer by a certain amount of Ni atoms owing to accelerated interdiffusion at the solid/liquid interface, while the formed Ni-based compound layers were continuously consumed until the transient liquid film contacted the HEC, as shown in Fig. 8(e).

The presence of the liquid film facilitated atomic interdiffusion between the HEC and Nb_2Ni layers. During this process, transition metal atoms in the HEC were released into the high melting point Nb_2Ni layer, particularly Ta atoms, and the Ni and Nb atoms in the Nb_2Ni layer diffused into the HEC. The remaining Ni atoms in the joint could be further homogenized. After a sufficient bonding time of 60 min, the metallurgically bonded HEC/Nb_2Ni interface shown in Fig. 8(f) formed in the joints.

In general, premised on the excellent high-temperature stability and sluggish diffusion effect of the HEC, the large interaction difference existed between the HEC/Ni interface and Nb/Ni interface, a formed Ni-Nb eutectic liquid film sequentially accelerated the *in situ* alloying of Nb and the interfacial diffusion between the HEC and the alloyed Nb_2Ni, resulting in the fabrication of a HEC joint with a high melting point Nb_2Ni layer at the diffusion bonding temperature that dramatically decreased to 1200–1250 °C. Notably, the bonding mechanism could not be applied to the joints in nonplanar components if it was difficult to apply uniform pressure at the bonding interface. Additionally, when conventional binary or composite ceramic substrates are applied, Ni-based phases remain at the interface due to the enhanced interaction between the conventional ceramics and the initial Ni layer during the diffusion-induced reaction stage, as shown in Figs. 8(a) and 8(b).

3.3 Mechanical properties of HEC joints bonded with a Ni/Nb/Ni composite interlayer

Figure 9 shows the effects of bonding temperature and interlayer type on the RT shear strength of the HEC joints. The joints with different interlayers of pure Nb, Nb-1, Nb-2, Nb-3, and pure Ni were diffusion bonded at 1200 °C under 10 MPa for 60 min, respectively. The strength improved from 126 to 174 MPa as the bonding temperature increased from 1150 to 1250 °C and increased from 133 to 204 MPa with increasing Ni thickness. Compared with the HEC/Nb/HEC diffusion-bonded joint, the HEC joints with a composite interlayer exhibited a substantial increase (4–6 times greater) in strength because the *in situ* alloying of Nb and the presence of the liquid film accelerated the interdiffusion at the bonding interface. The strength of the HEC/Nb-3/HEC diffusion-bonded joint was 35% greater than that of the HEC/Ni/HEC diffusion-bonded joint, which was probably attributed to the pinning effect of the eutectic liquid phase penetrating the ceramics at the interface [38] and the dispersion reinforcement effect of the fine NiNb phase in the IZ layer.

Figure 10 displays fracture macrographs and corresponding localized SEM images of the joints bonded at different temperatures. The HEC and the Nb-based interlayer could be viewed on the fracture surfaces, and the expanded area of HEC on the fracture with increasing bonding temperatures illustrated enhanced interfacial bonding. The EDS results of the exposed interfacial zones on the fractures from 1150 to 1250 °C are provided in Table S1 in the ESM. The Nb_2Ni phases with high Nb contents ranging from 53.33 to 57.46 at% were recognized by the fracture characteristics of the coarse grains and obvious grain boundaries in all the cases. The results indicated that joint failure occurred at the interface between the Nb_2Ni phase and the HEC.

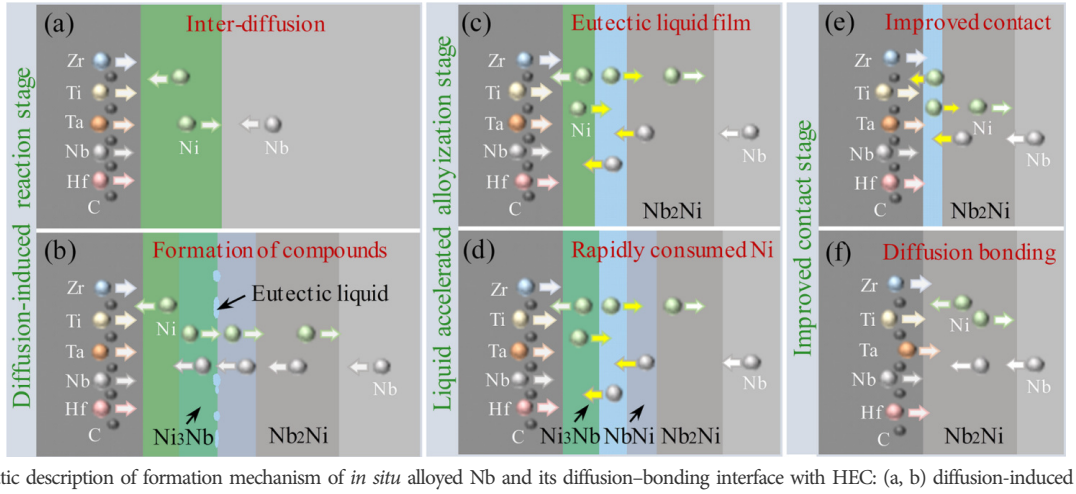

Fig. 8 Schematic description of formation mechanism of *in situ* alloyed Nb and its diffusion–bonding interface with HEC: (a, b) diffusion-induced reaction stage, (c, d) liquid accelerated alloyization stage, and (e, f) improved contact stage.

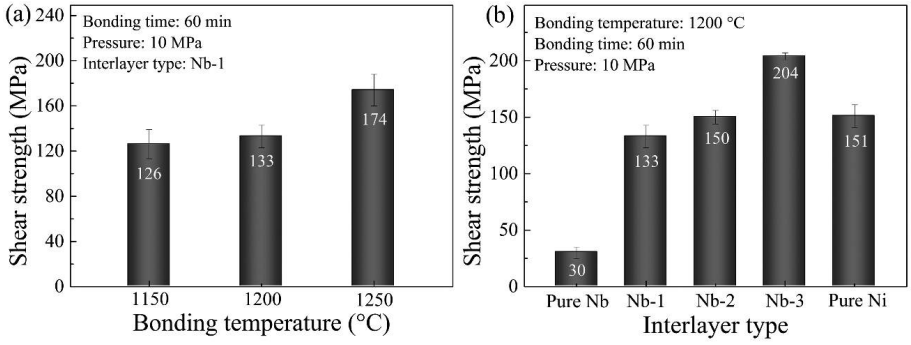

Fig. 9 Effects of bonding temperature and interlayer type on shear strength at RT of HEC joints obtained under 10 MPa for 60 min: (a) bonding temperature and (b) interlayer type.

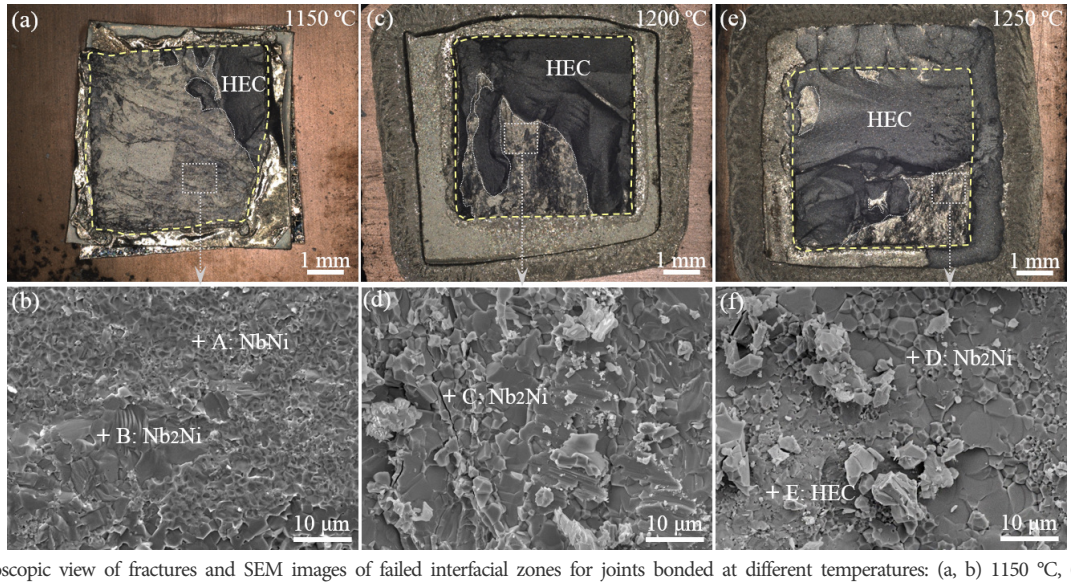

Fig. 10 Macroscopic view of fractures and SEM images of failed interfacial zones for joints bonded at different temperatures: (a, b) 1150 °C, (c, d) 1200 °C, and (e, f) 1250 °C.

At 1150 °C, a decreased Nb content of 46.00 at% and an increased Ni content of 34.25 at% were detected in the region with the appearance of fine pits in Fig. 10(b), which were assigned to the NbNi phase. This implied that the crack that occurred primarily in the Nb_2Ni layer propagated into the IZ layer in the joint. With increasing temperature, a large proportion of Nb_2Ni phases were observed, as shown in Figs. 10(d) and 10(f), indicating an identical weak zone in the joints.

From the nanohardness results of the phases in the HEC joints in Fig. 11, the nanohardness of Nb_2Ni (15.2±1.5 GPa) was between that of the pure Nb (5.7±0.2 GPa) and the HEC (36–39 GPa [2,39]). The elastic modulus of the phases also exhibited a similar trend. The formed Nb_2Ni layer provided a transition between the properties of soft Nb and the HEC, whereas its large brittleness and inconsistency deformation with the HEC still caused the failure of the HEC/Nb_2Ni interface when loaded. The alteration of the interfacial microstructure from a Nb_2Ni/Nb/Nb_2Ni layer to a homogeneous Nb_2Ni layer at an elevated bonding temperature of 1250 °C was beneficial for improving the joint strength because the mismatched elastic modulus between Nb and Nb_2Ni caused increased differences in the mechanical properties of the joint.

Figure 12 shows the macroscopic image and microstructure of shear fracture for the HEC/Nb-3/HEC joints bonded at 1200 °C. The exposed interfacial zone contained the Ni_3Nb phase and the HEC substrate, according to the EDS results in Table S2 in the ESM. The interface between the Ni_3Nb phase and the HEC was regarded as the failure position of the HEC/Nb-3/HEC joint. Compared with the HEC/Nb_2Ni interfacial structure shown in Fig. 6(a), the high strength of the HEC/Nb-3/HEC joint at RT benefited from the modified fracture pattern. The microstructure of the Ni_3Nb phase in Figs. 12(b) and 12(c) was characterized by a typical cleavage fracture, which was different from the intergranular fracture and coarse grains of the Nb_2Ni layer in Figs. 10(e) and 10(f). The larger number of Ni–Nb liquid phases generated in the HEC/Nb-3/HEC joint and penetration into the HEC substrate also favored enhanced interfacial bonding. Despite the slightly improved joint strength at RT, the increased Ni thickness resulted in the formation of a Ni_3Nb interlayer, which did not alleviate the deformation mismatch in the joint during loading. According to the results in Fig. 11, the nanohardness and elastic modulus of the Ni_3Nb phase were 13.9±1.6 GPa and 226.3±20.2 GPa, respectively, which approached those of the Nb_2Ni phase.

In Fig. 13(a), the high-temperature shear resistance of the joints with Nb-based interlayers was further investigated at temperatures up to 1000 °C. To directly visualize the high-temperature advantage of HEC joints with a Nb-based interlayer over a Ni-based interlayer under equivalent interfacial bonding states, the HEC/Nb-1/HEC joint with a diffusion-bonded interfacial structure between the Nb_2Ni layer and the HEC was adopted for comparison with HEC/Ni/HEC joints diffusion bonded at 1200 °C (shear strengths at RT of HEC/Ni/HEC joints under different bonding processes can be found in our previous work [15]). The

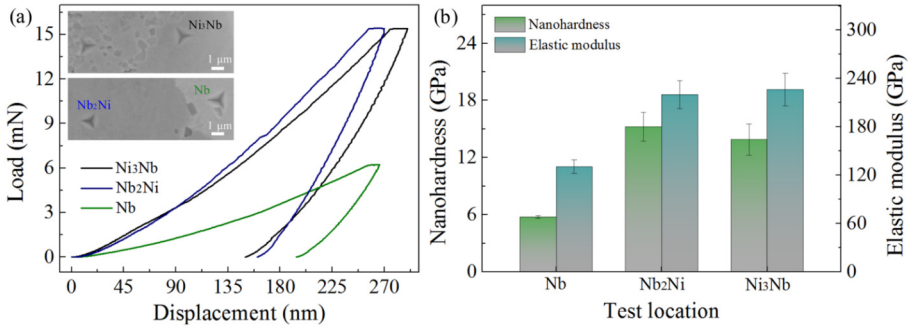

Fig. 11 Nanohardness results of phases in HEC joints bonded at 1200 °C: (a) typical load-displacement curves and corresponding test locations and (b) average nanohardness and elastic modulus.

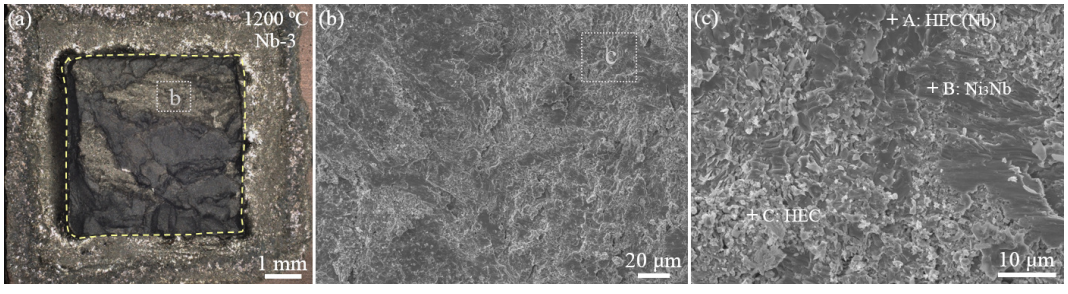

Fig. 12 Macroscopic and microstructure of shear fracture for HEC/Nb-3/HEC joints bonded at 1200 °C: (a) macroscopic view and (b, c) SEM images.

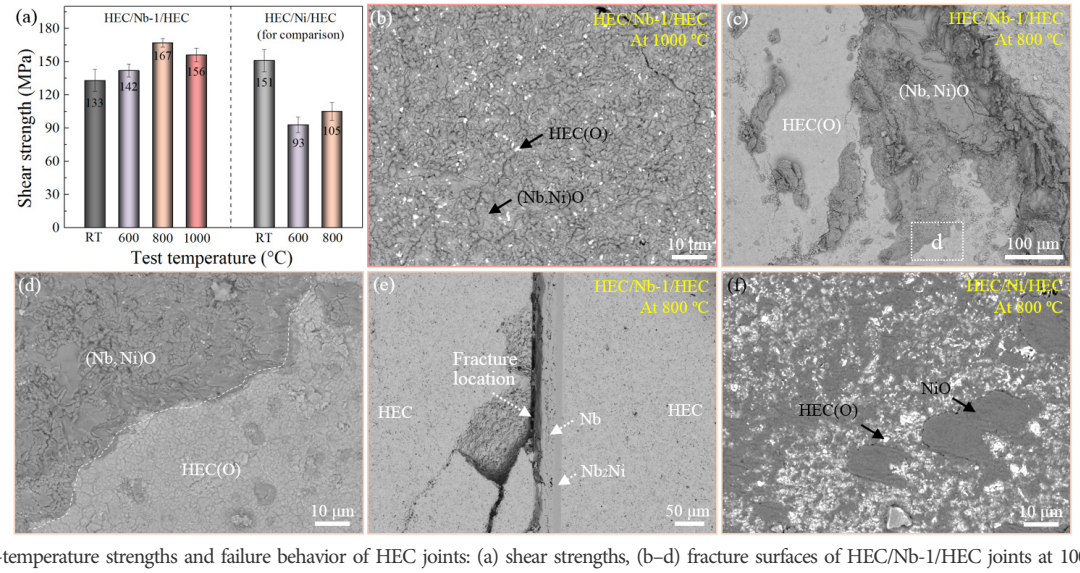

Fig. 13 High-temperature strengths and failure behavior of HEC joints: (a) shear strengths, (b–d) fracture surfaces of HEC/Nb-1/HEC joints at 1000 and 800 °C, respectively, (e) fracture path of HEC/Nb-1/HEC joint and (f) fracture surface of HEC/Ni/HEC joint at 800 °C.

results revealed that the HEC/Nb-1/HEC joints had undiminished strengths of 167 and 156 MPa when tested at 800 and 1000 °C, respectively. Compared with the RT strength of 133 MPa, the slightly increased strength values of the HEC/Nb-1/HEC joints were probably related to the release of internal stresses in the joints [24,40] and the enhanced plasticity of the Nb_2Ni layer at increased test temperatures. From the fracture surfaces in Figs. 13(b)–13(d), the oxidized Nb_2Ni phase with a 61.33 at% O content suggested that the failure of the HEC/Nb-1/HEC joint still occurred at the interface of Nb_2Ni and HEC, and the fracture path in Fig. 13(e) displayed a consistent result. The excellent high-temperature resistance to softening and oxidation of Nb_2Ni supported the high-temperature reliability of the HEC/Nb-1/HEC joints. It is foreseeable that the HEC joints are capable of serving at 1200 °C because the Nb-based interlayer, which has a high melting point above 1400 °C and good oxidation resistance, did not tend to soften.

In comparison, the strengths of the HEC/Ni/HEC joints significantly decreased from 151 MPa at RT to 105 MPa at 800 °C, as shown in Fig. 13(a). On the fracture of the HEC/Ni/HEC joints at 800 °C in Fig. 13(f), the large number of NiO zones with a large plastic rheological appearance reflected that a relatively poor resistance to high-temperature softening of the pure Ni interlayer was the reason for joint failure. These results further confirmed the unparalleled advantages of the refractory Nb-based interlayer formed *in situ* in the HEC joints for their high-temperature performance. The HEC joint with a Nb-based interlayer was favorable for higher operating temperatures (800–1200 °C) in oxidizing atmospheres than were the Ni-based interlayers for primary structural components and moderate thermal loads (≤

800 °C), which represented a breakthrough in the current bonding techniques for HECs to some extent.

4 Conclusions

In this study, on the basis of the excellent high-temperature stability and sluggish diffusion effect of the HEC at the bonding interface, the fabrication of HEC joints with improved high-temperature performance at decreased bonding temperatures of 1200–1250 °C was achieved by constructing an *in situ* alloyed refractory Nb-based interlayer and its eutectic liquid phase-assisted bonding interface with the HEC. The main conclusions included the following:

1) HEC joints with Nb-based interlayers relied on the *in situ* alloying of 60 μm Nb by 10 μm Ni at 1200–1250 °C under 10 MPa. The bonding structure of HEC/Nb_2Ni in the joint transformed into HEC/Ni_3Nb when the Ni/Nb proportion exceeded 36% or when the bonding temperature decreased excessively to 1150 °C. This phenomenon was the result of the inability to consume Ni even after the formation and extrusion of the eutectic liquid phase.

2) The HEC adjacent to the bonding interface maintained the original FCC high-entropy structure. The diffusion of Ta atoms from the HEC into the Nb_2Ni layer favored the interfacial bonding between the HEC and Nb_2Ni. The reliability of the HEC/Nb_2Ni interface was confirmed by a coherence of $(141)_{Nb_2Ni}//(1\bar{1}3)_{HEC}$ and a calculated lattice misfit of 0.044.

3) The HEC joint with a Nb_2Ni interlayer had a high RT strength of 171 MPa. Although failure at 1000 °C invariably occurred at the Nb_2Ni/HEC interface, the joint exhibited excellent high-temperature softening resistance from the nonweakened joint strength, and its strength was at least 49% greater than that of the HEC/Ni/HEC diffusion-bonded joint, which requires strict surface conditions.

Acknowledgements

The authors gratefully acknowledge the financial support from the National Natural Science Foundation of China (Nos. 52175357 and 52222511).

Declaration of competing interest

The authors have no competing interests to declare that are relevant to the content of this article.

Electronic Supplementary Material

Supplementary material is available in the online version of this article at https://doi.org/10.26599/JAC.2024.9221010.

References

[1] Pak AY, Sotskov V, Gumovskaya AA, *et al.* Machine learning-driven synthesis of $TiZrNbHfTaC_5$ high-entropy carbide. *NPJ Comput Mater* 2023, **9**: 7.

[2] Castle E, Csanádi T, Grasso S, *et al.* Processing and properties of high-entropy ultra-high temperature carbides. *Sci Rep* 2018, **8**: 8609.

[3] Li ZZ, Zhao ST, Ritchie RO, *et al.* Mechanical properties of high-entropy alloys with emphasis on face-centered cubic alloys. *Prog Mater Sci* 2019, **102**: 296–345.

[4] Oses C, Toher C, Curtarolo S. High-entropy ceramics. *Nat Rev Mater* 2020, **5**: 295–309.

[5] Cao ZN, Sun JL, Meng LT, *et al.* Progress in densification and toughening of high entropy carbide ceramics. *J Mater Sci Technol* 2023, **161**: 10–43.

[6] Sangiovanni DG, Kaufmann K, Vecchio K. Valence electron concentration as key parameter to control the fracture resistance of refractory high-entropy carbides. *Sci Adv* 2023, **9**: eadi2960.

[7] Peters AB, Zhang DJ, Chen S, *et al.* Materials design for hypersonics. *Nat Commun* 2024, **15**: 3328.

[8] Sun JL, Zhao J, Zhou YH, *et al.* High-performance multifunctional $(Hf_{0.2}Nb_{0.2}Ta_{0.2}Ti_{0.2}Zr_{0.2})C$ high-entropy ceramic reinforced with low-loading 3D hybrid graphene–carbon nanotube. *J Adv Ceram* 2023, **12**: 341–356.

[9] Dube TC, Zhang J. Underpinning the relationship between synthesis and properties of high entropy ceramics: A comprehensive review on borides, carbides and oxides. *J Eur Ceram Soc* 2024, **44**: 1335–1350.

[10] Wyatt BC, Nemani SK, Hilmas GE, *et al.* Ultra-high temperature ceramics for extreme environments. *Nat Rev Mater* 2023, **9**: 773–789.

[11] Wang RP, Wang G, Ran SL, *et al.* Microstructure and mechanical properties of C_f/SiC composite joints joined using $AlCoCrFeNi_{2.1}$ eutectic high-entropy alloy filler via spark plasma sintering. *J Eur Ceram Soc* 2023, **43**: 1853–1863.

[12] Wang XC, Saunders TG, Salvo M, *et al.* Joining graphite with ZrHfNbTa and TiZrHfTa high entropy alloy interlayers by spark plasma sintering. *J Mater Process Tech* 2023, **320**: 118102.

[13] Pan R, Lin TS, He P, *et al.* Design of the multiple transition metals interlayer process to diffusion bond ZrC_x ceramics. *Mater Design* 2018, **137**: 47–55.

[14] Pan R, Feng YH, Huang Z, *et al.* Microstructures and mechanical property of ZrC joints diffusion bonded using Ti/Ta/Ti as the interlayer. *J Eur Ceram Soc* 2023, **43**: 5830–5839.

[15] Mu RJ, Yang ZW, Niu SY, *et al.* Diffusion bonding of $(Hf_{0.2}Zr_{0.2}Ti_{0.2}Ta_{0.2}Nb_{0.2})C$ high-entropy ceramic with metallic Ni foil. *J Eur Ceram Soc* 2021, **41**: 7478–7487.

[16] Sun KB, Yang ZW, Mu RJ, *et al.* High-temperature stability of microstructure and mechanical properties of eutectic-reinforced high-entropy ceramic joint. *J Eur Ceram Soc* 2022, **42**: 4436–4445.

[17] Sun KB, Yang ZW, Mu RJ, *et al.* Active brazing of (HfTaZrNbTi)C high-entropy carbide ceramic and Nb with Ti Ni composite interlayer: Novel findings on the reaction layer. *Mater Charact* 2023, **203**: 113103.

[18] Sun KB, Yang ZW, Mu RJ, *et al.* Investigation of vacuum active brazing of (HfZrTiTaNb)C high-entropy carbide ceramic to Nb with TiZrCuNi filler alloy. *Vacuum* 2023, **215**: 112362.

[19] Wang PC, Xu ZQ, Qin B, *et al.* Active brazing of high entropy ceramic and Nb metal: Interfacial microstructure and brazing mechanism. *Vacuum* 2022, **205**: 111464.

[20] Silvestroni L, Sciti D, Esposito L, *et al.* Joining of ultra-refractory carbides. *J Eur Ceram Soc* 2012, **32**: 4469–4479.

[21] Liu GW, Zhang XZ, Yang J, *et al.* Recent advances in joining of SiC-based materials (monolithic SiC and SiC_f/SiC composites): Joining processes, joint strength, and interfacial behavior. *J Adv Ceram* 2019, **8**: 19–38.

[22] Lin JC, Zhou JF, Zhang SY, *et al.* Rapidly achieving a reliable full-ceramic interface of ZrC–SiC composite using Ti interlayer via pulsed electric current joining. *J Eur Ceram Soc* 2023, **43**: 1777–1789.

[23] Zhou L, Li F, Liu JX, *et al.* High-entropy $A_2B_2O_7$-type oxide ceramics: A potential immobilising matrix for high-level radioactive waste. *J Hazard Mater* 2021, **415**: 125596.

[24] Lin JC, Zhou JF, Yu D, *et al.* A new method for preparing high-strength and thermally-resistant ceramic/metal brazed joint at low temperature. *J Mater Res Technol* 2022, **20**: 1659–1664.

[25] Ong FS, Tobe H, Fujii G, *et al.* Microstructural evolution and mechanical characterization of Nb-interlayer-inserted Ti–6Al–4V/Si_3N_4 joints brazed with AuNiTi filler. *Mater Sci Eng A* 2020, **778**: 139093.

[26] Ye BL, Wen TQ, Huang KH, *et al.* First-principles study, fabrication, and characterization of $(Hf_{0.2}Zr_{0.2}Ta_{0.2}Nb_{0.2}Ti_{0.2})C$ high-entropy ceramic. *J Am Ceram Soc* 2019, **102**: 4344–4352.

[27] Chen BY, Li XF, Cui HL, *et al.* Investigation of tungsten/MA956 steel diffusion bonding with an Nb/Ni composite interlayer. *Int J Mod Phys B* 2020, **34**: 2050123.

[28] Zhou CY, Guo CP, Li JB, *et al.* Key experiments and thermodynamic

description of the Co–Nb–Ni system. *Metall Mater Trans A* 2020, **51**: 5892–5911.

[29] Zhao JF, Wang HP, Wei B. A modification of Nb-rich portion for refractory Nb–Ni alloy phase diagram with new peritectoid transition. *Metall Mater Trans A* 2023, **54**: 615–623.

[30] Afonso CRM, Martinez-Orozco K, Amigó V, *et al*. Characterization, corrosion resistance and hardness of rapidly solidified Ni–Nb alloys. *J Alloys Compd* 2020, **829**: 154529.

[31] Zhao JF, Li MX, Wang HP, *et al*. A kinetic transition from peritectic crystallization to amorphous solidification of rapidly quenched refractory Nb–Ni alloy. *Acta Mater* 2022, **237**: 118127.

[32] Wang H, Wang Z, Chen G, *et al*. Diffusion bonding of Zr–2.5Nb zirconium alloy and 304L stainless steel with Nb/Ni hybrid interlayer. *Mater Lett* 2022, **324**: 132652.

[33] Zheng LY, Li FZ, Zhou YC. Preparation, microstructure, and mechanical properties of TiB_2 using Ti_3AlC_2 as a sintering aid. *J Am Ceram Soc* 2012, **95**: 2028–2034.

[34] Birks LS, Seebold RE. Diffusion of Nb with Cr, Fe, Ni, Mo, and stainless steel. *J Nucl Mater* 1961, **3**: 249–259.

[35] Li PY, Jia YF, Yi JY, *et al*. Composition design, microstructure and mechanical properties of novel multiphase Ti–Cu–Ni–Nb complex concentrated alloys. *J Alloys Compd* 2020, **844**: 156175.

[36] Zhao JF, Wang HP, Wei B. A new thermodynamically stable Nb_2Ni intermetallic compound phase revealed by peritectoid transition within binary Nb–Ni alloy system. *J Mater Sci Technol* 2022, **100**: 246–253.

[37] Yang ZW, Zhang F, Yang X, *et al*. Microstructure and mechanical properties of Zr-4 alloy and 316 stainless steel diffusion bonding joint using Nb/Ni composite interlayer. *Adv Eng Mater* 2023, **25**: 2300279.

[38] Zhang XY, Lin JC, Wang W, *et al*. Directly construct a gradient brazed joint of SiC_f–SiC and Ni-based superalloy using a high-temperature AuCuV filler. *Mater Sci Eng A* 2022, **836**: 142722.

[39] Mu RJ, Wang Y, Niu SY, *et al*. Enhanced interfacial structure of (HfZrTiTaNb)C high-entropy ceramic joint brazed using $FeCoCrNiTi_{0.2}$ alloy filler. *J Mater Process Tech* 2024, **324**: 118253.

[40] Ong FS, Tobe H, Sato E. Simultaneous intermetallics suppression and residual-stress relaxation of heat-resistant Nb-interlayer-inserted Ti–6Al–4V/Si_3N_4 joints via one-step transient liquid phase bonding and brazing. *J Mater Sci Technol* 2023, **139**: 79–91.